

DOI: 10.1002/ ((please add manuscript number))

Article type: Full Paper

## Enhancing the Electrochemical Performance of Sodium-Ion Batteries by Building Optimized NiS<sub>2</sub>/NiSe<sub>2</sub> Heterostructures

*Shu-Ang He, Zhe Cui, Qian Liu\*, Guanjie He, Dan J. L. Brett Wei Luo\*, and Rujia Zou,\**

S. He, Z. Cui, Prof. W. Luo, Prof. R. Zou

State Key Laboratory for Modification of Chemical Fibers and Polymer Materials, College of Materials Science and Engineering, Donghua University, Shanghai 201620, P. R. China.

E-mail: wluo@dhu.edu.cn; rjzou@dhu.edu.cn

Prof. Q. Liu

E-mail: qianliu@dhu.edu.cn

Department of Physics, Donghua University, Shanghai 201620, P. R. China

Dr. G. He, Prof. D. Brett

Electrochemical Innovation Lab (EIL), Department of Chemical Engineering, University College London (UCL), London WC1E 7JE, UK

**Keywords:** NiS<sub>1.23</sub>Se<sub>0.77</sub> nanosheets, sulfide/selenide heterostructures, cavity structures, sodium-ion batteries, ultrahigh ICE

### Abstract

NiS<sub>1.23</sub>Se<sub>0.77</sub> nanosheets closely attached to the internal surface of hollow mesoporous carbon sphere (HMCS) to form a NiS<sub>1.23</sub>Se<sub>0.77</sub> nanosheets embedded in HMCS (NSSNs@HMCS) composite as the anode of sodium ion batteries (SIBs) is reported by a **facile** synthesis route. The anode exhibited a superior reversible capacity (520 mAh·g<sup>-1</sup> at 0.1 A·g<sup>-1</sup>), impressive coulombic efficiency (CE) of up to 95.3%, a high rate capacity (353 mAh·g<sup>-1</sup> at 5.0 A·g<sup>-1</sup>), excellent capacity retention at high current density (95.6%), and high initial coulombic efficiency (ICE) (95.1%). Firstly, the highest ICE for NiS<sub>2</sub>/NiSe<sub>2</sub>-based anode can be ascribed to ultrathin layered structure of NiS<sub>1.23</sub>Se<sub>0.77</sub> nanosheet and highly efficient electron transfer between the active material and HMCS. Secondly, the optimized NiS<sub>2</sub>/NiSe<sub>2</sub> heterostructure at the nanoscale of the inside HMCS was formed after the first discharge/charge cycles, which can provide rich heterojunction interfaces/boundaries of sulfide/selenides to offer faster Na<sup>+</sup> pathways, decrease the Na<sup>+</sup> diffusion barriers, increase electronic conductivity, and limit the dissolution of polysulfides or polyselenides in the electrolyte. Finally, the hollow structure of the HMCS accommodates the volume expansion, prevents the pulverization and aggregation issues of composite materials, which can also promote outstanding electrochemical performance.

## 1. Introduction

**Currently, it is urgent to promote carbon neutrality as a global goal due to the excessive consumption of earth resources and continuous deterioration of the environment. The clean and renewable energy storage devices (ESDs) are considered an important proportion of energy structure reform. Lithium-ion batteries (LIBs), with high energy density and excellent cycling stability, have been extensively applied as the power sources for various electronics and electric vehicles.** However, because of the high cost and resources required for LIBs, new candidates should be developed for energy storage technology. Recently, as an alternative to LIBs, sodium-ion batteries (SIBs) have attracted increasing attention as promising next-generation batteries owing to their low cost and widespread availability of sodium resources.<sup>[1,2]</sup> Nevertheless, the larger ionic radius (ca. 1.06 Å for Na versus ca. 0.76 Å for Li) and higher standard electrode potential (Na, -2.71 V versus standard hydrogen electrode (SHE); Li, -3.04 V versus SHE) of Na<sup>+</sup> cause serious issues for most electrode materials. The issues may be sluggish ion–electron transfer, high irreversible capacity, large volume change, which lead to a rapid capacity decay, and poor rate capability and low CE, which limit the commercial application of sodium batteries.<sup>[3,4]</sup>

In general, an ideal anode material for commercial application of SIBs should have high ICE, high CE, high rate capability, high specific capacity, and high capacity retention (called 5C requirements). At present, the anode materials are mainly classified into three groups based on their energy storage mechanism: intercalation-type (e.g., graphite, hard carbon),<sup>[5,6]</sup> alloy-type (e.g., P, Sb, Bi),<sup>[7-10]</sup> and conversion-type materials (e.g., Fe<sub>2</sub>O<sub>3</sub>, MoS<sub>2</sub>, FeSe<sub>2</sub>).<sup>[11-14]</sup> When compared with LIBs, the low reaction kinetics and large volumetric changes caused by the larger Na<sup>+</sup> are extremely significant in SIB electrodes with intercalation and alloy mechanisms during the charging/discharging process, causing the fast structural collapse of the electrodes. Therefore, the development of new electrode materials and new electrode structures with a low Na<sup>+</sup> diffusion barrier and high Na<sup>+</sup> storage for SIBs should be strongly encouraged, which can satisfy the 5C requirements. In previous studies,<sup>[15-19]</sup> transition metal sulfides (TMS) and selenides (TMSe) based on conversion-type chemistries have been regarded as promising anode materials owing to their large theoretical capacity, suitable interlayer distance, appropriate working potential, low diffusion energy barriers, and designable fast transfer path of ion/electron, which yields high performance in SIBs. However, the intrinsically physical features of the low intrinsic electrical conductivity and large volume variation caused pulverization and structural changes in the TMS and TMSe anode materials during cycling processes. Besides, the irreversible decomposition of Na<sub>2</sub>S or Na<sub>2</sub>Se and phase structural

transformation caused by the “shuttle” effect of polysulfides/polyselenides inhibits  $\text{Na}^+$  diffusion and induces capacity decay during cycling processes. These critical drawbacks of TMS and TMSe lead to rapid capacity decay, poor rate capability, and low CE, which limit the practical applications of SIBs.<sup>[20-23]</sup> To date, significant efforts have been devoted to overcome these issues, and the electrochemical performance of TMS/TMSe electrodes has been significantly improved. Hybridization of carbon materials with graphene, carbon nanotubes, carbon fibers, and porous carbon has been widely employed to enhance the electrical conductivity of TMS and TMSe. This demonstrated synergy toward shortening electron paths, boosting structure stability, and accommodating volume changes, which allow for excellent rate performance and cycling stability.<sup>[24-26]</sup> Furthermore, controlling the morphology with two-dimensional metal sulfides/selenides or layered structure materials to shorten the ion diffusion pathway is also widely designed to decrease the sodium diffusion barrier and accommodate the volume expansion. However, the slow kinetics and low CE significantly hinder achieving excellent rate performance and cycle performance, particularly at high current densities. Recently, heterostructure engineering has been demonstrated as a most promising strategy to enhance the electrode performance. The constructed heterostructure can tune the electronic structure and result in higher electron delocalization, which can improve the electron conductivity of the anode materials.<sup>[27]</sup> Moreover, the phase boundaries of the heterostructure could provide broad migration paths and lower the diffusion energy barrier for  $\text{Na}^+$ .<sup>[28]</sup> Rational bond strength can induce reversible reactions during charge/discharge processes. These functions primarily concentrate on building high reaction kinetics and facilitating charge transport for SIBs, which can obtain high-rate performance and cycle performance. Although heterostructure engineering has been successful in extending the electrochemical performance of anode materials, the increased phase boundaries in heterostructures might lead to further side reactions for electrolyte consumption and irreversible  $\text{Na}^+$  trapping, which results in a low ICE of heterostructure materials and significantly decrease lifespan of the electrode. More importantly, the synthesis of heterostructures with rich phase boundaries under optimized conditions still remains a significant challenge.

Herein, we report the synthesis of  $\text{NiS}_{1.23}\text{Se}_{0.77}$  nanosheets embedded in hollow mesoporous carbon spheres (NSSNs@HMCS) and their application as anode materials in SIBs for the first time. This application of NSSNs@HMCS can address or alleviate the aforementioned problems to satisfy the 5C requirements. Based on theoretical calculations, it was found that the introduction of a smaller proportion of Se atoms into the  $\text{NiS}_2$  crystal can yield an optimal electronic structure and enhance the electrical conductivity of the anode

materials. The thin layer of  $\text{NiS}_{1.23}\text{Se}_{0.77}$  nanosheets was transformed into optimized TMS/TMSe heterostructures on the internal surface of the HMCS after the first discharge process, which can avoid side reactions with excessive electrolyte consumption, resulting in an ultrahigh ICE for TMS/TMSe-based anodes. Then, we found that optimized TMS/TMSe heterostructures with rich phase boundaries were formed to build a high diffusion channel for  $\text{Na}^+$  in the composite materials in the discharge process, which can obtain high reaction kinetics and facilitate charge transport for SIB. In addition, the irreversible decomposition of  $\text{Na}_2\text{S}$  or  $\text{Na}_2\text{Se}$  and possible dissolution of polysulfides/polyselenides into the electrolyte were also alleviated by the heterostructures during cycling. Finally, the hollow mesoporous carbon sphere can accommodate the volume expansion, and prevent the pulverization and aggregation issues of composite materials during cycling, thereby further promoting durable stability and high CE. The experimental results demonstrated that the NSSNs@HMCS electrodes in SIBs exhibit outstanding ICE, CE, rate capability, specific capacity, and capacity retention.

## 2. Result and Discussion

### 2.1. Materials and Characterization

The synthesis process of NSSNs@HMCS is schematically illustrated in **Figure 1**. First, yolk-shell partially hollow mesoporous carbon spheres (PHMCS) were produced via pyrolysis and a partial etching process (Figure S1). Then, a simple chemical deposition was applied to grow the  $\text{Ni}(\text{OH})_2$  nanosheets inside the interspace of the yolk-shell PHMCS nanospheres, obtaining the  $\text{SiO}_2$ @ $\text{Ni}(\text{OH})_2$  nanosheets@HMCS nanostructure (Figure S2). Finally, yolk-shell NSSNs@HMCS were synthesized by the anion exchange process, and the internal  $\text{SiO}_2$  spheres were completely etched under alkaline conditions after the hydrothermal reaction. For comparison, the yolk-shell  $\text{NiS}_2$  nanosheets embedded in HMCS (NSNs@HMCS) and  $\text{NiSe}_2$  nanosheets embedded in HMCS (NSENs@HMCS) were constructed by modifying the ratio of the sulfur and selenium powders of the hydrothermal reaction (Figure S3 and S4). The  $\text{NiS}_{1.23}\text{Se}_{0.77}$  nanoparticles embedded in HMCS (NSSNP@HMCS) was constructed by directly calcining the NSSNs@HMCS nanostructure (Figure S5). Herein, the partially etched  $\text{SiO}_2$  nanospheres for the synthesis process play a critical role in the successful structural design of NSSNs@HMCS: (1) the inner  $\text{SiO}_2$  spheres can serve as growth substrates for the  $\text{Ni}(\text{OH})_2$  nanosheets owing to the strong adsorption of metal ions caused by the functional groups located on their surface (Figure S6 shows the SEM image of the growth of  $\text{Ni}(\text{OH})_2$  in HMCS); (2) the interspace between HMCS and  $\text{SiO}_2$  nanospheres is key to the formation of the thin layer structure of  $\text{NiS}_{1.23}\text{Se}_{0.77}$  nanosheet to improve ICE performance; (3) the remaining space

following the etching process can accommodate the volume change during the charging/discharging process.

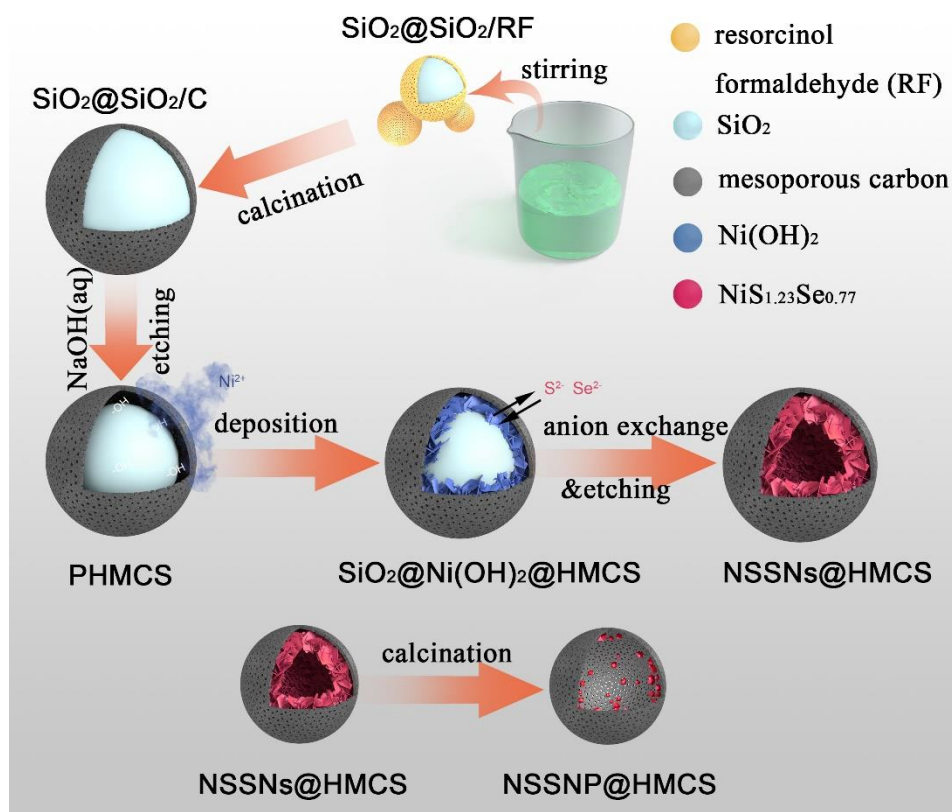


**Figure 1.** Schematic illustration of the synthesis process of NSSNs@HMCS and control group of NSSNP@HMCS.

Morphological observations of NSSNs@HMCS were conducted using scanning electron microscope (SEM) and transmission electron microscope (TEM) at different magnifications. As shown in **Figure 2a**, the SEM image reveals that  $\text{SiO}_2@\text{Ni}(\text{OH})_2$  nanosheets@HMCS nanospheres with a uniform diameter between 260 and 300 nm were obtained, which are the same size as the original yolk-shell PHMCS nanospheres. The TEM image (Figure 2b) reveals that the  $\text{Ni}(\text{OH})_2$  nanosheets grow in the interspace of the yolk-shell PHMCS nanospheres to form the  $\text{SiO}_2@\text{Ni}(\text{OH})_2$  nanosheets@HMCS structure. As shown in Figure 2c, NSSNs@HMCS nanospheres were obtained via the anion-exchange process and complete etching of the  $\text{SiO}_2$  spheres. In addition, the carbon spheres possess a mesoporous feature, which helps in the transfer and penetration kinetics of  $\text{Na}^+$  and other electrolyte components. In Figure 2d **and S7**, the  $\text{NiS}_{1.23}\text{Se}_{0.77}$  nanosheets with a few-layer structure were first obtained from the  $\text{Ni}(\text{OH})_2$  nanosheets via the anion exchange process. The layer thickness of the  $\text{NiS}_{1.23}\text{Se}_{0.77}$  nanosheets was 5–8 nm. The ultrathin layer of  $\text{NiS}_{1.23}\text{Se}_{0.77}$  nanosheets was tightly attached to the inner surface of the carbon shells, which also enhanced the electrical

conductivity of the composite materials (as shown in Figure 2e). The high-resolution transmission electron microscopy (HRTEM) image and corresponding selected area electron diffraction (SAED) pattern of NSSNs@HMCS are shown in Figure 2f. The HRTEM image and SAED pattern reveal that the nanosheets have clear lattice fringes separated by 0.26, 0.22, and 0.26 nm, corresponding to the (102), (022), and ( $\bar{1}20$ ) crystal planes of  $\text{NiS}_{1.23}\text{Se}_{0.77}$  (JCPDS 04-002-6935). Furthermore, the corresponding EDS elemental mapping images (Figure 2g and S8) reveal the distribution of C, Ni, S, and Se elements. The distribution area of the elements is a strong contrast of the looping structure, indicating a core-shell structure of the NSSNs@HMCS. The Brunauer–Emmett–Teller (BET) analysis was conducted to survey the surface area and pore structure of NSSNs@HMCS, as presented in Figure S9. The nitrogen adsorption–desorption isotherm demonstrates its type IV adsorption–desorption feature with a type H<sub>4</sub> hysteresis loop following the International Union of Pure and Applied Chemistry classification, which is characteristic of porous carbon and stacked nanosheets (inset of Figure S9). Owing to its ultrathin nanosheets hybridized with porous carbon structure, the specific surface area of NSSNs@HMCS is calculated to be  $372.7 \text{ m}^2 \text{ g}^{-1}$  and its total pore volume and diameter of pore size are approximately  $1.9 \text{ cm}^3 \text{ g}^{-1}$  and 7.808 nm, respectively. Such a large specific area is useful for the penetration of the electrolyte and  $\text{Na}^+$  storage.

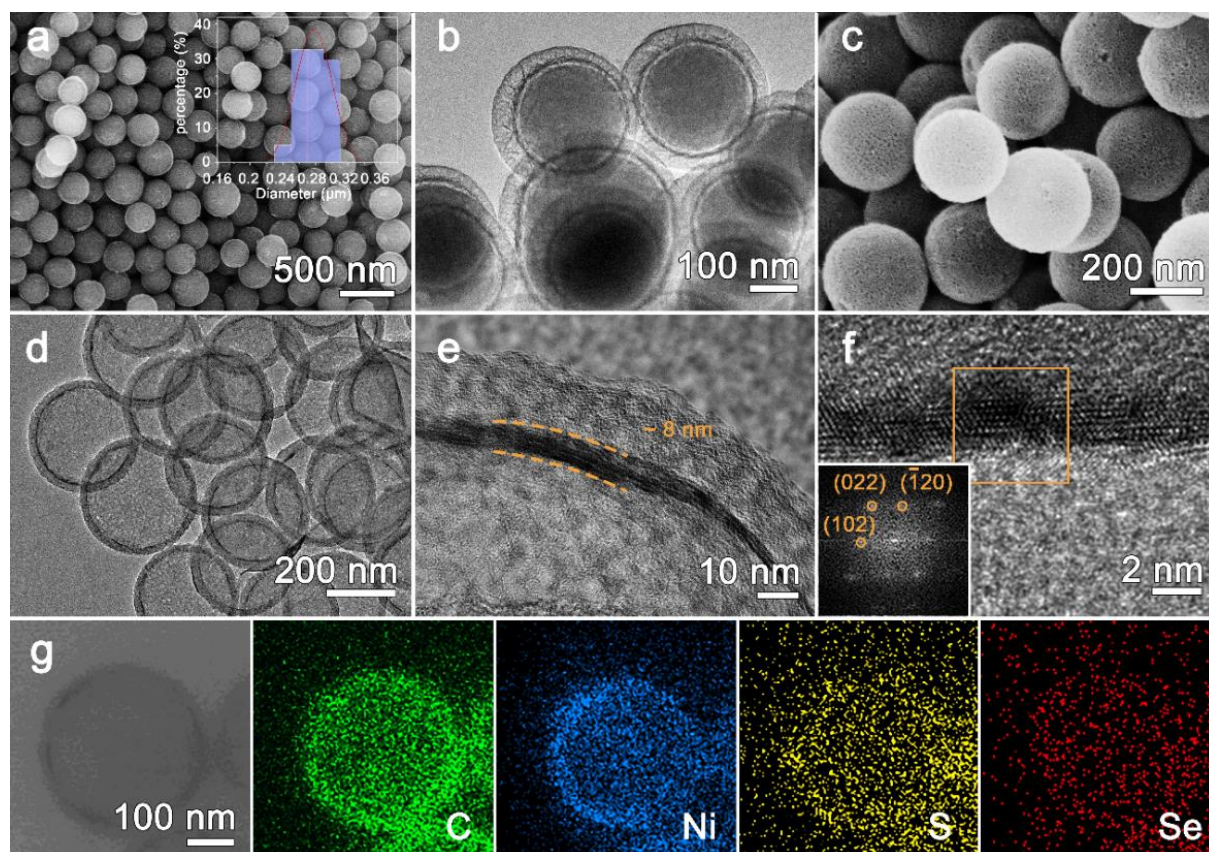


**Figure 2.** (a) SEM images of  $\text{SiO}_2@\text{Ni}(\text{OH})_2@\text{HMCS}$  and the inset presents the particle size statistics. (b) TEM images of  $\text{SiO}_2@\text{Ni}(\text{OH})_2@\text{HMCS}$ . (c) SEM image of  $\text{NSSNs}@\text{HMCS}$ . (d) and (e) TEM images of  $\text{NSSNs}@\text{HMCS}$  at the different magnification. (f) HRTEM images of  $\text{NSSNs}@\text{HMCS}$  and the inset is corresponding FFT pattern. (g) STEM image and the corresponding EDS element mapping images of  $\text{NSSNs}@\text{HMCS}$ .

**Figure 3a** shows the X-ray diffraction (XRD) pattern of the  $\text{NSSNs}@\text{HMCS}$  sample. This reveals that the patterns at  $30.9^\circ$ ,  $34.7^\circ$ ,  $38.1^\circ$ ,  $44.3^\circ$ ,  $52.5^\circ$ ,  $57.5^\circ$ , and  $59.9^\circ$  correspond to the (200), (210), (211), (220), (311), (023), and (321) lattice planes of cubic  $\text{NiS}_{1.23}\text{Se}_{0.77}$  (JCPDS 04-002-6935), while the broad peak around  $2\theta \approx 26^\circ$  corresponds to the carbonaceous shells, suggesting that the obtained sample is  $\text{NSSNs}@\text{HMCS}$ . The XRD patterns of  $\text{NiS}_{1.23}\text{Se}_{0.77}$  show an intensity mismatch, which implies that the layered structure of  $\text{NiS}_{1.23}\text{Se}_{0.77}$ , corresponding to the analysis derived from the TEM images. In addition, the characteristic peaks of  $\text{NiS}_2$  (JCPDS 65-3325) and  $\text{NiSe}_2$  (JCPDS 65-1843) were obtained, confirming that the  $\text{NSNs}@\text{HMCS}$  and  $\text{NSeNs}@\text{HMCS}$  were synthesized after modifying the ratio of the sulfur and selenium powders (Figure S10a). The Raman spectra of  $\text{NSSNs}@\text{HMCS}$  confirmed the chemical constitution, as shown in Figure 3b. When compared with  $\text{NSNs}@\text{HMCS}$  and  $\text{NSeNs}@\text{HMCS}$  samples, the Raman peaks of  $\text{NSSNs}@\text{HMCS}$  located at approximately 251, 374, and  $467\text{ cm}^{-1}$  for  $A_g$  (stretching) mode of Se-Se pairs, S-Se pairs, and S-S pairs, respectively, which indicate the presence of the  $\text{NiS}_{1.23}\text{Se}_{0.77}$ .<sup>[20,29]</sup> **For  $\text{NSSNs}@\text{HMCS}$ ,  $\text{NSNs}@\text{HMCS}$ , and  $\text{NSeNs}@\text{HMCS}$ , the presence of graphitic carbon was confirmed by the Raman peaks of the two conventional peaks at  $1355$  and  $1588\text{ cm}^{-1}$  (Figure S10c).**

Figure 3c–e display the X-ray photoelectron spectroscopy (XPS) spectra of  $\text{NSSNs}@\text{HMCS}$  and control groups, which provide further information about the surface electron state and electronic structure. The survey scan (Figure S11 and Table S1) reveals the existence of the C, Ni, S, and Se elements with the atomic ratio of nearly 1:1.23:0.77, which strongly supports the successful preparation of  $\text{NiS}_{1.23}\text{Se}_{0.77}$ . The Ni 2p spectrum can be divided into two groups of characteristic peaks at 880.7/875.4/873.9 and 863.1/857.9/856.7 eV (Figure 3c), corresponding to the Ni 2p<sub>1/2</sub> and Ni 2p<sub>3/2</sub>, respectively. The peaks at 873.9/856.7 and 875.4/857.9 eV are attributed to the Ni-Se and Ni-S bonds, respectively.<sup>[30,31]</sup> When compared with the binding energies of the  $\text{NSNs}@\text{HMCS}$  and  $\text{NSeNs}@\text{HMCS}$ , the Ni-S bonds shifted negatively and Ni-Se bonds shifted positively in the Ni 2p spectrum, indicating that the electronic structure of the  $\text{NSSNs}@\text{HMCS}$  has been effectively modified by adjusting the ratio of S:Se. This is important for improving conductivity of materials, which is discussed below.

Moreover, the peaks of Ni 2p spectrum at 879.8/862.6 eV indicate the satellite peaks. The distinct peaks located at the binding energy of 162.4/161.1 and 165.4/164.1 eV corresponding to the S-Ni and S-S bonds, in the S 2p spectrum (Figure 3d).<sup>[32,33]</sup> The peak at 167.3 eV suggests the S-O bonds that originated from the oxidation in air. In Figure 3e, Se 3d spectrum shows the peaks at 54.7, 55.8, and 59.3 eV, assigned to the Se-Ni, Se-Se/Se-S, and Se-O bonds.<sup>[34,35]</sup> Finally, the contents of active material in the samples were investigated using the thermogravimetric analysis (TGA) in air, as shown in Figure 3f. The TGA results of NSSNs@HMCS, NSNs@HMCS, and NSeNs@HMCS show that the samples tend to completely decompose to NiO at approximately 600 °C in air.<sup>[36]</sup> Therefore, the weight ratio with active material of NiS<sub>1.23</sub>Se<sub>0.77</sub>, NiS<sub>2</sub>, and NiSe<sub>2</sub> in NSSNs@HMCS, NSNs@HMCS, and NSeNs@HMCS are calculated to be 92.3%, 70.8%, and 77.8%, respectively. Such high mass loading of active material in of NSSNs@HMCS is the preferable nanostructured design, demonstrating great promise for electrochemical energy storage (EES) systems with high energy density and power density.

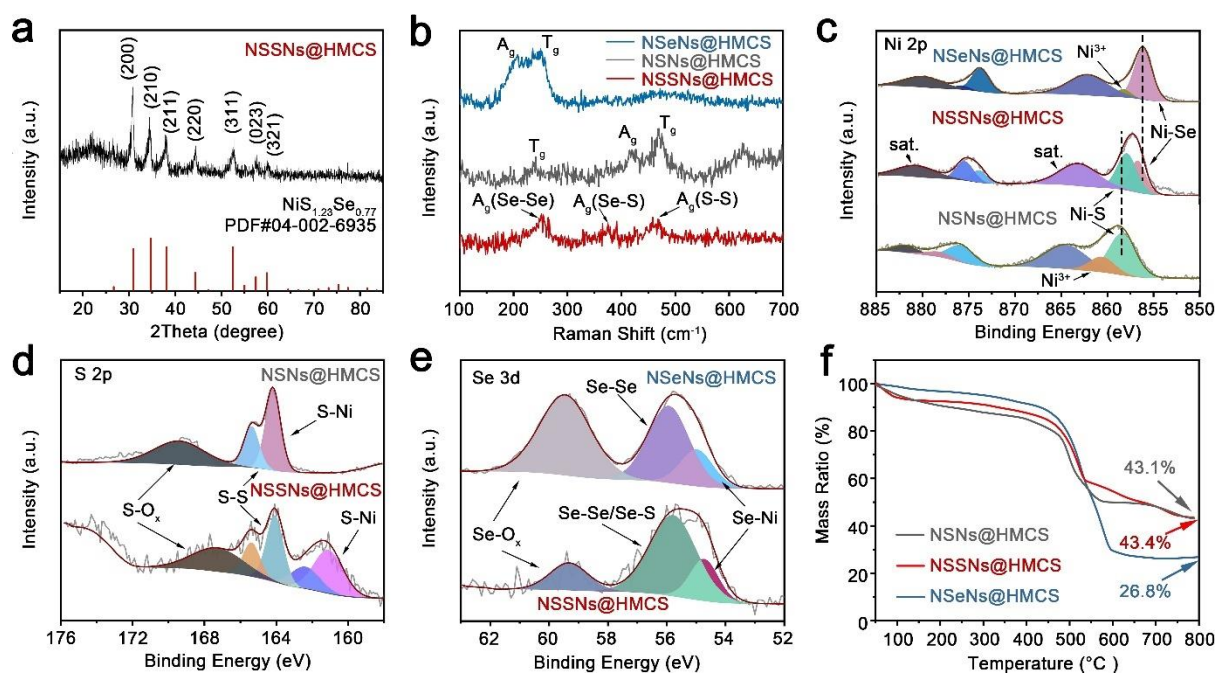


**Figure 3.** (a) XRD patterns of the NSSNs@HMCS. (b) **Raman spectra of NSSNs@HMCS, NSNs@HMCS, and NSeNs@HMCS.** (c–e) High resolution XPS spectrums of Ni 2p, S 2p, and Se 3d for NSSNs@HMCS, NSNs@HMCS, and NSeNs@HMCS. (f) The TG curves of NSSNs@HMCS, NSNs@HMCS, and NSeNs@HMCS.

## 2.2 Electrochemical Performance

The electrochemical behaviors were investigated through galvanostatic charge–discharge cycling experiments in coin cells in the potential range of 0.01–3.0 V, as shown in **Figure 4**. The cycling voltammetry (CV) measurement of NSSNs@HMCS electrode was applied at the sweep rate of 0.1 mVs<sup>-1</sup> at a voltage window of 0.01–3.0 V versus Na<sup>+</sup>/Na. The initial five cycles of the CV curves are shown in Figure 4a. In the first cathodic sweep, two peaks located at approximately 0.53, and 0.30 V can be detected and disappear in the subsequent scans, corresponding to the formation of a solid electrolyte interface (SEI) film. Two reduction peaks at approximately 1.24 and 0.90 V and four oxidation peaks at approximately 1.53, 1.62, 1.89, and 2.1 V can be observed, which suggest the NiS<sub>1.23</sub>Se<sub>0.77</sub> undergoes multistep reactions during the sodiation/desodiation process. The intercalation and conversion reactions are sequentially activated as the cathodic scan progresses. The peaks at approximately 1.53 and 1.89 V are assigned to the formation of NiSe<sub>2</sub>, and the peaks at approximately 1.62 and 2.1 V are attributed to the formation of NiS<sub>2</sub>, which are consistent with the previous reports.<sup>[24,37,38]</sup> A pair of redox peaks near 0.01 V might be attributed to the pseudo-capacitive process at the interface of the formed nanoparticles.<sup>[39]</sup> In the second cycle, the cathodic peaks at approximately 1.24 and 0.9 V shift positively to approximately 1.58 and 1.01 V, and the anodic peaks at approximately 1.89 and 2.1 V shift negatively to approximately 1.82 and 1.96 V, which are caused by the enhanced electrochemical kinetics of electrode after the first cycle owing to the formation optimized material structure. The profiles of subsequent cycles remained steady and overlapped well, indicating that the electrochemical reaction was reversible and stable.<sup>[40]</sup> The galvanostatic charge/discharge profiles of the NSSNs@HMCS electrode during the initial five cycles at a current density of 0.1 A·g<sup>-1</sup> are displayed in Figure 4b. The discharge plateaus at approximately 1.5 and 1.0 V coincide with the locations of peaks presented in CV curves. All peaks shown in the differential charge and discharge capacity versus voltage plots were consistent with the CV analysis (Figure S12). The NSSNs@HMCS electrode delivered high initial first discharge and charge capacities of approximately 837 and 815 mAh·g<sup>-1</sup>, respectively, corresponding to an ICE (ICE) of approximately 97.4%. Interestingly, the NSSNs@HMCS electrode delivered an ultrahigh ICE when compared with the other control sample electrodes (Figure S13) and previously reported (supporting information Table S2) alloy-type and conversion-type materials. Then, the discharge capacities decreased to 646 and 610 mAhg<sup>-1</sup> in the second and third cycles, respectively, corresponding to a CE of approximately 97.4% and 97.4%, respectively, which indicates the formation of a stable SEI. The high ICE of the NSSNs@HMCS electrode is attributed to the layered structure for the formation of a stable SEI before the conversion reaction during the first discharge process, according to the CV curves,

which can provide protection against restraint side reactions for consumption electrolyte and unrecoverable active material and  $\text{Na}^+$ . In addition, the high electronic conductivity of the electrode materials also results in a high ICE and CE. As shown in Figure S14, the density of states (DOS) of  $\text{NiS}_2$ ,  $\text{NiS}_{1.5}\text{Se}_{0.5}$ ,  $\text{NiSSe}$ ,  $\text{NiSe}_2$ , and  $\text{NiS}_{1.25}\text{Se}_{0.75}$ , were simulated using the CASTEP package. As a result, the largest density of states near the Fermi level when the S:Se ratio is 1.25:0.75, which implies highly efficient electron mobility in  $\text{NiS}_{1.25}\text{Se}_{0.75}$ . Here, the S:Se ratio of  $\text{NiS}_{1.23}\text{Se}_{0.77}$  in NSSNs@HMCS is closest to that of  $\text{NiS}_{1.25}\text{Se}_{0.75}$ , which leads to rapid electronic transport to obtain a high ICE and CE.

The rate performances of the NSSNs@HMCS, NSNs@HMCS, NSeNs@HMCS, and NSSNP@HMCS electrodes at various current densities are shown in Figure 4c. The NSSNs@HMCS electrode delivers the highest specific capacities with the average discharge capacities of 556, 473, 452, 420, 390, and 353  $\text{mAh}\cdot\text{g}^{-1}$  under the current density of 0.1, 0.2, 0.5, 1.0, 2.0, and 5.0  $\text{A}\cdot\text{g}^{-1}$ , respectively. Further, the specific capacity rapidly recovered to 450.9  $\text{mAh}\cdot\text{g}^{-1}$  when the rate switched to 0.1  $\text{A}\cdot\text{g}^{-1}$ , implying the good structure stability of the NSSNs@HMCS electrode under high current density. As shown in Figure 4c, the NSSNs@HMCS electrode has a higher rate performance than that of NSSNP@HMCS, which further verifies that the layered structure of the  $\text{NiS}_{1.25}\text{Se}_{0.75}$  nanosheets exhibits low electrolyte consumption and high  $\text{Na}^+$  diffusion behavior, enhancing the ICE and CE to improve the rate performance. The cycle stability of NSSNs@HMCS electrode was evaluated at a current density of 0.1  $\text{A}\cdot\text{g}^{-1}$  up to 60 cycles, as shown in Figure 4d. The discharge capacity was approximately 610  $\text{mAh}\cdot\text{g}^{-1}$  for the fourth cycle (first three cycles to enable the formation of a stable SEI layer), which was maintained at 499  $\text{mAh}\cdot\text{g}^{-1}$  after 60 cycles, exhibiting an impressive specific capacity. Furthermore, excellent durability at high current densities is critical for anode materials in SIB electrodes. The long-term cycling stabilities of the NSSNs@HMCS, NSNs@HMCS, NSeNs@HMCS, and NSSNP@HMCS electrodes at a current density of 2  $\text{A}\cdot\text{g}^{-1}$  are shown in Figure 4e. Among the four electrodes tested, the NSSNs@HMCS electrode delivered the highest cycling stability, maintaining 95.6% of its initial capacity of 405  $\text{mAh}\cdot\text{g}^{-1}$  after 1500 cycles. The capacities of NSNs@HMCS, NSeNs@HMCS, and NSSNP@HMCS were 308, 339, and 71  $\text{mAh}\cdot\text{g}^{-1}$  after 200 cycles, respectively. The NSSNs@HMCS electrode shows a decaying capacity rate of 0.003% for every cycle, which is the lowest capacity fading rate among the four electrodes, and also lower than those previously reported for  $\text{NiS}_2$ -based and  $\text{NiSe}_2$ -based electrodes at high current densities.<sup>[24,37,41-43]</sup> In addition, the CE of the NSSNs@HMCS electrode was almost 100% during the cycles, which is much higher than that of NSNs@HMCS, NSeNs@HMCS, and

NSSNP@HMCS. From the optical photographs of the back of the electrodes after the cycles, it can be seen that the NSSNs@HMCS electrode remained bright, while the NSeNs@HMCS and NSNs@HMCS electrodes were corroded to varying degrees (Figure S15). The NSSNs@HMCS electrode exhibits outstanding capacity and cycling stability at a high current density of  $2 \text{ A}\cdot\text{g}^{-1}$ , which fits well with the current demand for rapid battery charging technology and may help the SIBs to be used in actual commercial applications.

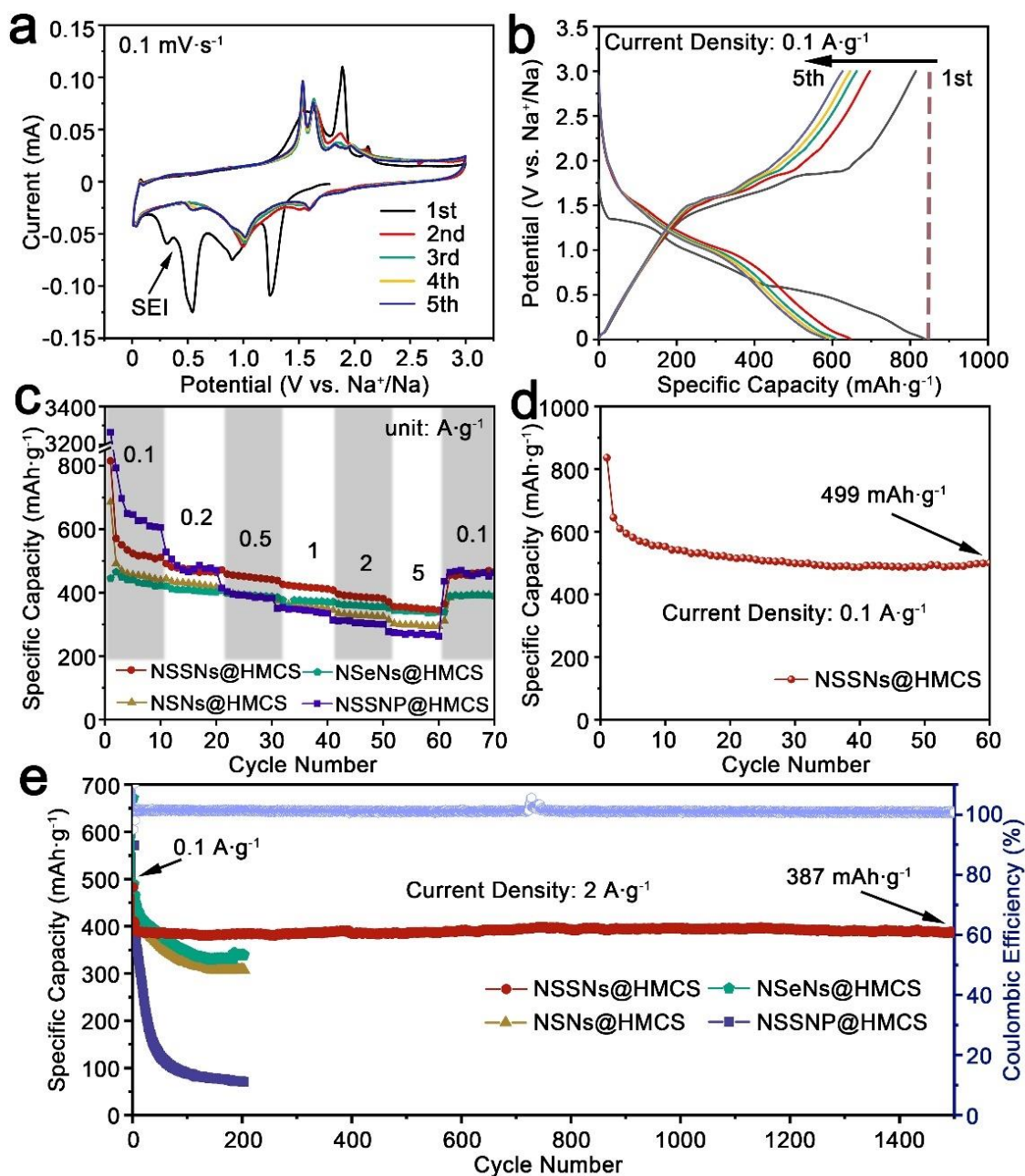


**Figure 4.** (a) CV curves of NSSNs@HMCS electrode in the initial five scans with a scan rate of  $0.1 \text{ mV}\cdot\text{s}^{-1}$ . (b) GCD profiles of NSSNs@HMCS electrode during the initial five cycles at a current density of  $0.1 \text{ A}\cdot\text{g}^{-1}$ . (c) Rate performance of NSSNs@HMCS, NSNs@HMCS, NSeNs@HMCS, and NSSNP@HMCS. (d) Cycling stability of NSSNs@HMCS at  $0.1 \text{ A}\cdot\text{g}^{-1}$ . (e) High-current density performance of NSSNs@HMCS, NSNs@HMCS, NSeNs@HMCS, and NSSNP@HMCS at  $2 \text{ A}\cdot\text{g}^{-1}$ .

NSeNs@HMCS, and NSSNP@HMCS electrodes under different current rates, respectively. (d) Cycling performance of NSSNs@HMCS electrode under a current density of  $0.1 \text{ A}\cdot\text{g}^{-1}$ . (e) Cycling performance of NSSNs@HMCS, NSNs@HMCS, NSeNs@HMCS, and NSSNP@HMCS electrodes at a high current density of  $2 \text{ A}\cdot\text{g}^{-1}$ .

### 2.3 Sodiation/Desodiation Mechanism

The anode material for SIBs suffers from serious volume change, low utilization, and sluggish kinetics during the charge/discharge process, particularly at high current densities. Therefore, the electrochemical behavior, reaction mechanism, and kinetics of electrode materials are key factors to develop SIBs with high energy densities, excellent rate performance, and superior long cycling stability. To reveal the electrochemical behavior, reaction mechanism, and kinetics of NSSNs@HMCS during the sodiation/desodiation process, a series of measurements and theoretical simulations were conducted. Therefore, *ex situ* Raman spectra and TEM accompanied by the fast Fourier transform (FFT) were employed to probe the evolution of morphology and phase during sodiation and desodiation processes. For the *ex situ* Raman analysis, several typical point positions of A–G were selected for testing during the first discharge/charge process, as presented in **Figure 5a**. The curve of A is the pristine electrode before the discharge/charge process, curves of D and G are the electrode after complete charge/discharge process, curves of B and E are the beginning of plateaus, and curves of C and F are the end of the plateaus. For curve A, there are three peaks at approximately  $250$ ,  $378$  and  $462 \text{ cm}^{-1}$ , which can be ascribed to Se-Se, S-Se, and S-S pairs, indicating the presence of  $\text{NiS}_{1.23}\text{Se}_{0.77}$ . The two peaks gradually weakened during the discharge process (curve B). Then, the two peaks completely disappeared when the electrode was fully discharged (curves C and D), indicating the complete conversion of  $\text{NiS}_{1.23}\text{Se}_{0.77}$ . Subsequently, a reverse reaction process is observed during the charging process. The two peaks gradually appeared during the charging process (curves E and F). **When the electrode was fully charged (curve G), there are two distinct peaks at approximately  $210 \text{ cm}^{-1}$  and  $460 \text{ cm}^{-1}$ , the peak positions are changed comparing with the peaks of the pristine electrode at approximately  $250 \text{ cm}^{-1}$  and  $467 \text{ cm}^{-1}$ . And comparing with curve A the peak represented S-Se disappear, indicating the full conversion from  $\text{NiS}_{1.23}\text{Se}_{0.77}$  to  $\text{NiS}_2/\text{NiSe}_2$  composite.** The *ex situ* TEM measurements provided further evidence that the material phase structure and component of  $\text{NiS}_{1.23}\text{Se}_{0.77}$  were transformed during the first discharge/charge process, as illustrated in Figure 5b–e. After the sodiation process was completed, it can be seen that the nanosheets are converted to nanoparticles on the inner surface of carbon shells. After the desodiation process was completed,

the matrix layer of the active material adsorbed closely to the inner surface of the HMCS, significantly improved the ion/electron transfer kinetics and structural stability. The HRTEM images and FFT analysis in Figure 5d show that the matrix layer of active materials is confirmed to consist of NiS<sub>2</sub> and NiSe<sub>2</sub> ultrafine nanoparticles with sizes of 5–10 nm to form an optimized NiS<sub>2</sub>/NiSe<sub>2</sub> heterostructure. Furthermore, the *in situ* TEM experiment was employed to investigate the sodiation and desodiation processes (Figure S16), which was consistent with the above results. *In situ* TEM observations further suggest that the NiS<sub>1.23</sub>Se<sub>0.77</sub> transforms into NaS<sub>2</sub>/NaSe<sub>2</sub> composites after the discharge process and then transforms into NiS<sub>2</sub>/NiSe<sub>2</sub> composites after charge processes inside the HMCS structure. The thin matrix layer of the NiS<sub>2</sub>/NiSe<sub>2</sub> heterostructure maintained close contact with the robust HMCS structure, which provides highly efficient pathways for fast electron/ion transfer during charging/discharging processes. Here, the following three strategically interdependent characteristics of the self-formation of the optimized NiS<sub>2</sub>/NiSe<sub>2</sub> heterostructure from NiS<sub>1.25</sub>Se<sub>0.75</sub> nanosheets are responsible for improving the electrochemical behavior, reaction mechanism, and reaction kinetics. First, forming the rich heterojunction interfaces/boundaries of sulfide/selenides at the nanoscale can offer faster Na<sup>+</sup> pathways and decrease the Na<sup>+</sup> diffusion barriers during the cycle process, which can significantly improve the reaction kinetics for the anode of SIBs. Second, the thin matrix layer of the homogeneous NiS<sub>2</sub>/NiSe<sub>2</sub> heterostructure on the inner surface of the HMCS greatly increases the electronic conductivity between the NiS<sub>2</sub>/NiSe<sub>2</sub> heterostructure and HMCS, which can facilitate the electrochemical reaction between Na<sup>+</sup> and the active materials. Third, the homogeneous NiS<sub>2</sub>/NiSe<sub>2</sub> heterostructure is beneficial for limiting the phase transformation and decreasing the dissolution of polysulfides or polyselenides into the electrolyte during cycling, which can promote CE, rate capacity, and cycle life during cycling processes.

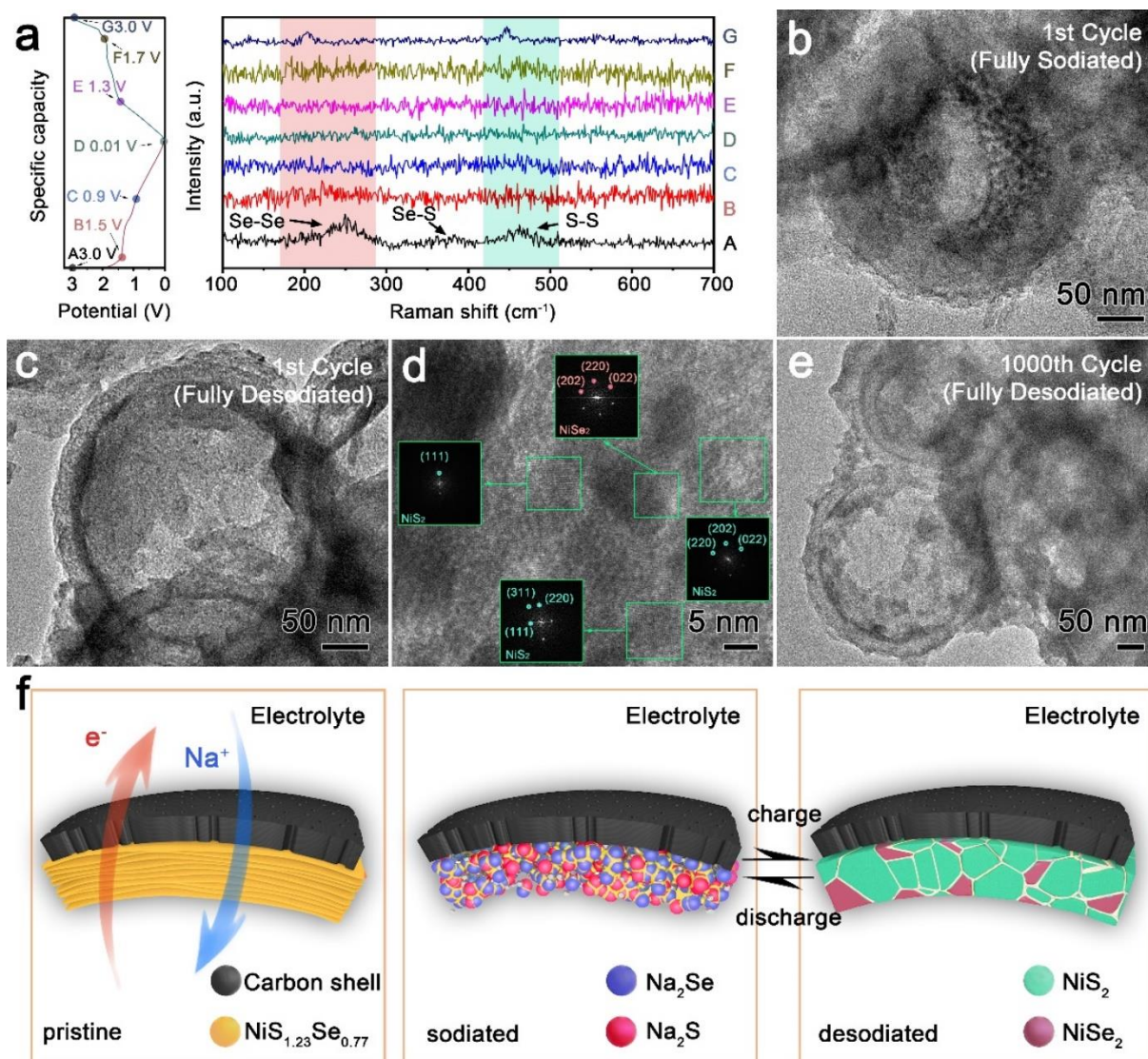


**Figure 5. (a) The voltage-time curves and *ex situ* Raman spectra of NSSNs@HMCS electrode at different charge/discharge stages during the first cycle process. (b and c) TEM images of NSSNs@HMCS electrode after fully sodiated to 0.01 V vs.  $\text{Na}^+/\text{Na}$  and fully desodiated to 3.0 V vs.  $\text{Na}^+/\text{Na}$ . (d) HRTEM image and FFT patterns of NSSNs@HMCS electrode after fully desodiated process. (e) Morphology of fully charged NSSNs@HMCS electrode after 1000 discharge/charge cycles. (f) Schematic of the electrode morphology evolution during discharge/charge process.**

To further demonstrate the improvement in the electrochemical behavior, reaction mechanism, and kinetics of the optimized  $\text{NiS}_2/\text{NiSe}_2$  heterostructure, a series of electrochemical kinetics and quantitative analyses were also performed. **Figure 6a** displays CV curves with an increasing scan rate from 0.1 to  $4.0 \text{ mV}\cdot\text{s}^{-1}$  to investigate the electrochemical kinetics mechanism of the NSSNs@HMCS electrode as the SIB anode. The CV curves of

NSSNs@HMCS, NSNs@HMCS, and NSeNs@HMCS electrodes display similar shapes, implying small polarization and superb stability, as shown in Figures 6a and S17. The capacity of the electrode consists of the diffusion contribution and capacitance contribution. To quantitatively analyze the proportion of the capacitance contribution, the following formulas between the peak current ( $i$ ) and scan rate ( $v$ ) were applied: [44,45]

$$i = av^b \quad (1)$$

$$\log(i) = b\log(v) + \log(a) \quad (2)$$

where  $a$  and  $b$  are two variable parameters. The  $b$  value can be obtained by fitting the slope of  $\log(i)$  and  $\log(v)$  from Equation (2). When the  $b$  value varies in the range of 0.5 to 1, the dominant contributor of capacity changes from a diffusion-controlled process to a surface-controlled (pseudocapacitive) process. Through linear fitting, the  $b$  values of peaks 1 and 2 in both cathodic and anodic processes for the three electrodes were 0.96, 0.96, 0.76, and 0.88, 0.80, and 0.71, respectively, indicating that the electrodes all include diffusion-controlled and pseudocapacitive mechanisms (Figure 6b). More accurately, the capacitance contributions can be quantified using the following equation:

$$i(V) = k_1v + k_2v^{1/2} \quad (3)$$

where  $k_1v$  represents the pseudocapacitive contribution, and  $k_2v^{1/2}$  corresponds to the diffusion contribution. The proportions of the pseudocapacitive contributions for the three electrodes are shown in Figure 6c. The pseudocapacitive contributes 82% of the capacity for NSSNs@HMCS electrode at a low scan rate of  $0.1 \text{ mV}\cdot\text{s}^{-1}$ , and this ratio gradually increases as the scan rate increases, reaching 96.6% at  $4.0 \text{ mV}\cdot\text{s}^{-1}$ , which is much higher than those of the NSNs@HMCS (77.4% at  $0.1 \text{ mV}\cdot\text{s}^{-1}$  and 95.6% at  $4.0 \text{ mV}\cdot\text{s}^{-1}$ ) and NSeNs@HMCS (51.4% at  $0.1 \text{ mV}\cdot\text{s}^{-1}$  and 87.0% at  $4.0 \text{ mV}\cdot\text{s}^{-1}$ ) electrodes. This result indicates that the NSSN@HMCS electrode with high pseudocapacitive contribution possesses good reversibility due to large amounts of heterojunction interfaces/boundaries by self-formation of optimized  $\text{NiS}_2/\text{NiSe}_2$  heterostructures, while maintaining an excellent cycle stability and large capacity at high current density during the cycling process. Furthermore, according to the Randles-Sevcik equation, the linear fitting slope between the peak currents and the square root of the scan rate is proportional to the ion diffusion coefficient. Figure 6d displays the fitting results, and the largest slope value of the NSSNs@HMCS electrode reveals faster ion transfer, which may be ascribed to the shortened ion pathway and excellent reaction kinetics. The galvanostatic intermittent titration technique (GITT) was carried out to further investigate the diffusion coefficient of  $\text{Na}^+$ , which was calculated based on the simplified equation as follows: [46]

$$D_{Na^+} = \frac{4}{\pi\tau} \left( \frac{m_B V_m}{M_B S} \right)^2 \left( \frac{\Delta E_s}{\Delta E_\tau} \right)^2 \left( \tau \ll \frac{L^2}{D} \right) \quad (4)$$

where  $D_{Na^+}$  is the diffusion coefficient,  $m_B$  is the active mass of the electrode,  $V_m$  is the molar volume,  $M_B$  is the molar mass of the electrode,  $S$  is the electrochemically active area of the electrode,  $\Delta E_s$  is the difference in open-circuit voltages after two adjacent relaxations, and  $\Delta E_\tau$  is the voltage difference between the beginning and termination of a single pulse step. As shown in Figure 6e, the estimated diffusion coefficient depends on the charge status, showing a downward trend with the discharge/charge as a whole and mainly ranges from  $10^{-15}$  to  $10^{-11}$   $\text{cm}^2 \text{s}^{-1}$ . In addition, the diffusion coefficient is usually restricted by the phase reaction such as the rapid decrease at around 1.5 V and 1.3 V in the discharge process and 1.5 V and 1.8 V in the charging process, coinciding with the cathodic and anodic peaks shown in CV curves, respectively. It can be seen that the NSSNs@HMCS electrode exhibits the highest ion diffusion coefficient and the lowest *in situ* reaction resistance during the charge/discharge process owing to the homogeneous NiS<sub>2</sub>/NiSe<sub>2</sub> heterostructures by self-formation at the nanoscale to increase fast ion/electron transfer, limit phase transformation, and decrease the dissolution of polysulfides or polyselenides into the electrolyte during cycling (Figure 6f), further indicating the fast reaction kinetics in sodium storage, resulting in excellent cycling durability and rate capability.

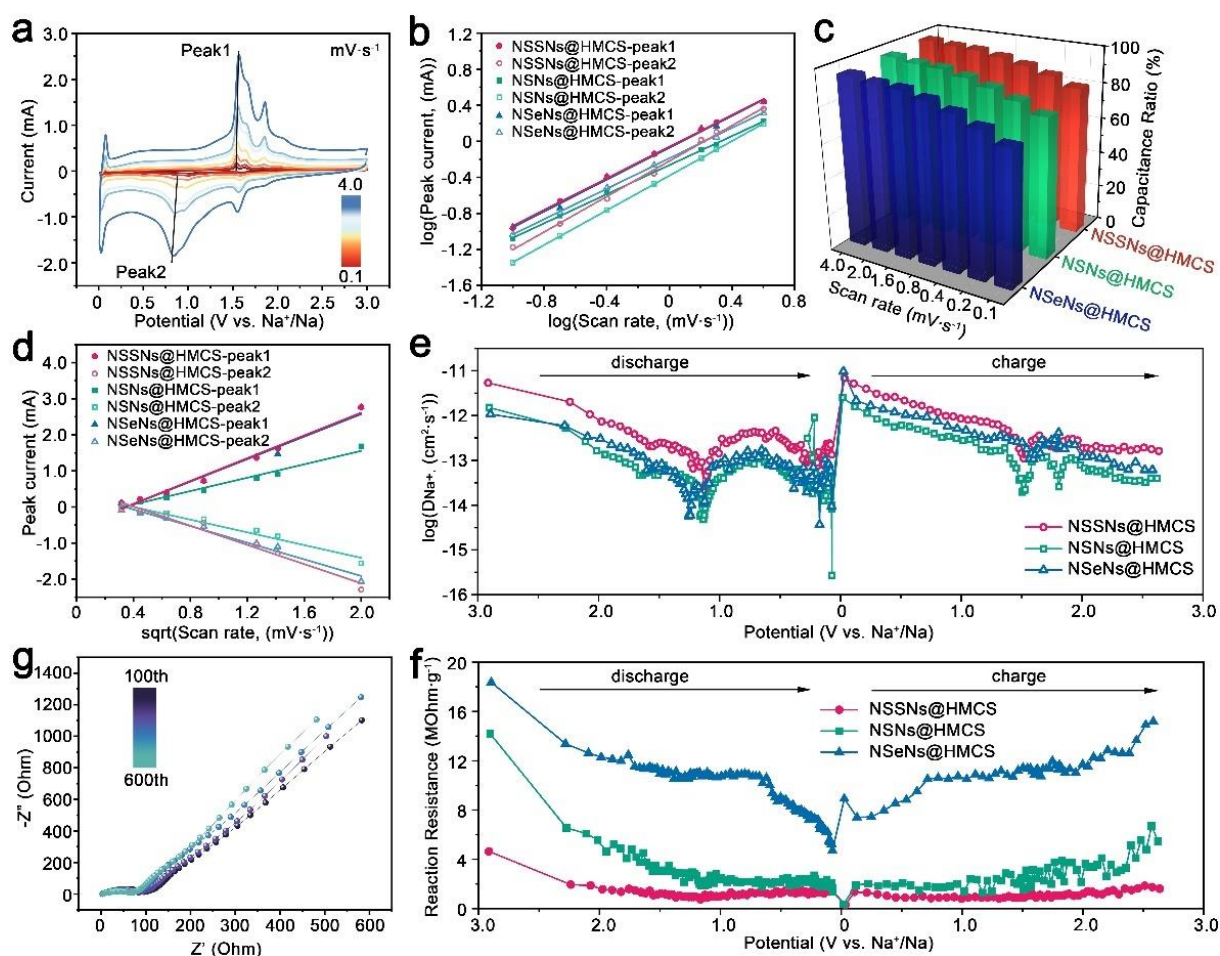


**Figure 6.** (a) CV curves of NSSNs@HMCS electrode at different scan rates varied from 0.1 to 4.0  $\text{mV}\cdot\text{s}^{-1}$ . (b) The linear relationship of peak currents and scan rates of NSSNs@HMCS, NSNs@HMCS, and NSeNs@HMCS electrodes. (c) Normalized ratios of surface capacitive contributions for NSSNs@HMCS, NSNs@HMCS, and NSeNs@HMCS electrodes at various scan rates. (d) The linear relation between the square root of scan rates and peak currents for the peak1 and peak2 indicating in the CV curves of NSSNs@HMCS, NSNs@HMCS, and NSeNs@HMCS electrodes. (e) Diffusion coefficient estimated from GITT charge/discharge profile for sodiation and desodiation. (f) In-situ reaction resistance during the discharge/charge process calculated by GITT measurement. (g) Nyquist plots of NSSNs@HMCS electrode after 100, 200, 300, and 600 cycles.

Finally, electrochemical impedance spectroscopy (EIS) shows the resistance evolution of the NSSNs@HMCS electrode during the long cycling process (Figure 6g). It can be seen that the resistance maintains stability from the 100th to 600th cycle, which further demonstrates the prominent structural stability and ionic diffusion behavior of self-formation homogeneous  $\text{NiS}_2/\text{NiSe}_2$  heterostructures. Furthermore, according to the TEM and SEM images (Figure 5e and S18), the active materials were found to be closely attached to the inner surface of the

HMCS during discharge/charge cycles. As a result, the NSSN@HMCS remained well without any apparent destruction after 1000 cycles at a high current density. A sufficient and well-defined internal void space of HMCS is key to maintaining the structural integrity of NSSNs@HMCS, which is also favorable for the formation of uniform NiS<sub>2</sub>/NiSe<sub>2</sub> heterostructures. Overall, the above characterization results proved that the NSSN@HMCS electrode with 5C requirements for the anode of SIBs can be attributed both to the materials used and their structural design.

### 3. Conclusion

In summary, the NSSN@HMCS composite of NiS<sub>1.23</sub>Se<sub>0.77</sub> nanosheets formed on the internal surface of HMCS was successfully fabricated as an anode for SIBs. The highly interconnected NSSN@HMCS composite with layered NiS<sub>1.23</sub>Se<sub>0.77</sub> nanosheets and highly efficient electron mobility of NiS<sub>1.23</sub>Se<sub>0.77</sub> established a protection against restraint side reactions for consumption electrolyte, unrecoverable active material and Na<sup>+</sup>, and efficient charge-transfer channels, which can contribute to the high ICE. More importantly, we also demonstrated that the optimized NiS<sub>2</sub>/NiSe<sub>2</sub> heterostructure on the inner surface of the HMCS was built after the first discharge/charge process by combining *ex situ* Raman and *ex situ* TEM characterization. The electrochemical kinetics and quantitative analysis revealed that the homogeneous nanoscale NiS<sub>2</sub>/NiSe<sub>2</sub> heterostructure on the inner surface of HMCS can generate rich heterojunction interfaces/boundaries of sulfide/selenides, offer more fast Na<sup>+</sup> pathways, decrease the Na<sup>+</sup> diffusion barriers, increase the electronic conductivity, and limit the irreversible dissolution of polysulfides or polyselenides into the electrolyte during cycling, which can promote CE, rate capacity, and cycle life during cycling. Finally, the void spaces effectively accommodate the volume expansion of the anode materials without rupturing the HMCS. The NSSN@HMCS composite exhibited an ultrahigh ICE of 95.1%, high CE (up to 100%), and superior rate capacity performance (510 mAh·g<sup>-1</sup> at 0.1 A·g<sup>-1</sup> and 428 mAh·g<sup>-1</sup> at 5.0 A·g<sup>-1</sup>), excellent cycling durability of 405 mAh·g<sup>-1</sup> after 1500 cycles at 2 A·g<sup>-1</sup> (capacity retention of 95.6%). Our work revealed an efficient approach to promote the electrochemical performance of SIB anodes by reasonable structure design and unique electronics adjustment strategy and shed new light on exploring the superior performance anode of 5C requirements for SIBs.

## 4. Experimental Section

### Materials

$\text{Ni}(\text{Ac})_2 \cdot 4\text{H}_2\text{O}$ , hexamethylenetetramine (HMT), resorcinol, formaldehyde (37 wt %), ammonia ( $\text{NH}_3 \cdot \text{H}_2\text{O}$ , 25 wt %), ethanol, sodium hydroxide (NaOH), sodium sulfide ( $\text{Na}_2\text{S} \cdot 9\text{H}_2\text{O}$ ), deionized (DI) water, tetraethylorthosilicate (TEOS), selenium (Se) powder, sulfur (S) powder, 1-methyl-2-pyrrolidinone (NMP), super P, and polyvinylidene difluoride (PVDF) were purchased from Aladdin without any purification treatment. The electrolyte solution with 1 M  $\text{NaPF}_6/1,2$ -dimethoxyethane (DME) were supplied by Guangdong Canrd New Energy Technology Co., Ltd..

### **Synthesis of Partially Hollow Mesoporous Carbon Spheres (PHMCS)**

In a typical synthesis method, 3.46 mL of TEOS was added to the solution containing 70 mL ethanol, 10 mL DI water, and 3 mL of ammonia solution under vigorous stirring at room temperature. After 10 min, 0.6 g of resorcinol and 0.84 mL formaldehyde were added to the above solution, and this solution was kept under vigorous stirring for 24 h at room temperature. The precipitates were collected by centrifugation, washed with DI water and ethanol, and then dried in vacuum oven at 60 °C overnight, and the  $\text{SiO}_2@\text{SiO}_2/\text{resorcinol}$  formaldehyde ( $\text{SiO}_2@\text{SiO}_2/\text{RF}$ ) was obtained. Afterward, the brick red precipitates were calcinated in a tube furnace filled with nitrogen to 700 °C with 2 °C·min<sup>-1</sup> of heating rate for 5 h to obtain  $\text{SiO}_2@\text{SiO}_2/\text{C}$  nanospheres. Finally, the  $\text{SiO}_2@\text{SiO}_2/\text{C}$  nanospheres were process by 80 mL of 1 M NaOH solution under room temperature to etched silica partially, then the PHMCS were obtained.

### **Synthesis of Yolk-Shell $\text{SiO}_2@\text{Ni}(\text{OH})_2$ Nanosheets@Hollow mesoporous carbon ( $\text{SiO}_2@\text{Ni}(\text{OH})_2$ nanosheets@HMCS)**

First, 0.236 g of  $\text{Ni}(\text{Ac})_2 \cdot 4\text{H}_2\text{O}$  and 0.14 g of HMT were dissolved into the solution containing 61 mL of DI water and 5 mL ethanol to form a transparent solution under ultrasonic dispersion for 30 min. Then, 0.1 g of PHMCS were added into above solution under vigorous stirring. After further stirring for 30 min, the system was transferred into a 100 mL Teflon-lined stainless-steel autoclave, and kept in a 100 °C oven for 10 h. Afterward, the product was collected by centrifugation, washed with DI water and ethanol, and dried at 60 °C overnight. The yolk-shell  $\text{SiO}_2@\text{Ni}(\text{OH})_2$  nanosheets@HMCS was obtained.

### **Synthesis of Yolk-Shell $\text{NiS}_{1.23}\text{Se}_{0.77}$ Nanosheets@HMCS (NSSNs@HMCS)**

1.12 g of Sulfur powder, 25 mg of selenium powder, and 2.4 g of  $\text{Na}_2\text{S} \cdot 9\text{H}_2\text{O}$  were mixed and dissolved in 40 mL DI water under vigorous stirring at 80 °C. Then, 160 mg of as-prepared  $\text{SiO}_2@\text{Ni}(\text{OH})_2@\text{HMCS}$  were added into the solution. After stirring for 30 min, the solution was transferred to a 100 mL Teflon-lined stainless-steel autoclave and maintain at 160 °C for 24 h. The black precipitates were washed with DI water and ethanol several times to remove

residual reactant and by-product before freeze drying, the yolk-shell  $\text{NiS}_{1.23}\text{Se}_{0.77}$  nanosheets@HMCS was obtained.

### **Synthesis of Yolk-Shell $\text{NiS}_2$ Nanosheets@HMCS (NSNs@HMCS) and Yolk-Shell $\text{NiSe}_2$ Nanosheets@HMCS (NSeNs@HMCS)**

As control materials, the yolk-shell  $\text{NiS}_2$  nanosheets@HMCS and  $\text{NiSe}_2$  nanosheets@HMCS were synthesized by using 1.25 g of S powder or 1.54 g of Se powder and 2.4 g of  $\text{Na}_2\text{S}\cdot 9\text{H}_2\text{O}$  to prepare the precursor solution, respectively.

### **Synthesis of $\text{NiS}_{1.23}\text{Se}_{0.77}$ Nanoparticles@HMCS (NSSNP@HMCS)**

The  $\text{NiS}_{1.23}\text{Se}_{0.77}$  nanoparticles@HMCS was obtained by heating the  $\text{NiS}_{1.23}\text{Se}_{0.77}$  nanosheets@HMCS in a tube furnace at 400 °C for 2 h under nitrogen.

### **Materials Characterization**

Field-emission scanning electron microscopy (FESEM, Hitachi S-4800) and high-resolution transmission electron microscopy (TEM, JEOL JEM-2100F equipped with an energy-dispersive X-ray spectrometer) were performed to investigate the morphologies and structures of samples. Powder XRD patterns were collected using an X-ray diffractometer D/MAX-2550VB+ to confirm the components and the phases of the composites. XPS data was conducted to explore chemical valence states, which were obtained in an EALALab MIKII spectrometer with an excitation source of Mg-K $\alpha$  radiation. The carbon content of sample has been studied by the thermogravimetric analysis (TGA, Libra/209F1). Nitrogen adsorption-desorption isotherms were collected by an autosorb-iQ device. To prepare the cycled electrodes for ex situ SEM, TEM, and Raman characterization, the cycled cells were taken apart in an argon-filled glovebox and then carefully washed by acetonitrile to remove the residual electrolyte. After drying, they were sealed in Kapton tape for measurement.

### **Electrochemical Measurements**

The electrochemical performances were tested in half 2032 coin-type cells with metal sodium foil as the counter electrode and reference electrode. The work electrodes were prepared by mixing active materials ( $\text{NiS}_{1.23}\text{Se}_{0.77}$  nanosheets@HMCS,  $\text{NiS}_2$  nanosheets@HMCS,  $\text{NiSe}_2$  nanosheets@HMCS,  $\text{NiS}_{1.23}\text{Se}_{0.77}$  nanoparticles@HMCS, and  $\text{NiS}_{1.23}\text{Se}_{0.77}$  nanosheets), super P, and PVDF in weight ratios of 7:2:1 with NMP as solvent. Glass fiber membrane (Guangdong Canrd New Energy Technology Co., Ltd.) as the separator. The organic electrolyte for half-cells is composed of 1 M  $\text{NaPF}_6$  /DME, active materials loading was 1.0-1.2  $\text{mg}\cdot\text{cm}^{-2}$ . The fabrication of coin cells was completed in an argon-filled glovebox (with both the moisture and the oxygen concentration below 0.1 ppm). Galvanostatic discharge-charge measurement and

GITT were performed on a LANHE battery testing system (LAND2001A) within 0.01-3.0 V. Cyclic voltammetry (CV, voltage range from 0.01 V to 3.0 V) and electrochemical impedance spectroscopy (EIS, frequency range from **100 kHz** to 0.01 Hz) were tested on an Autolab (PGSTA302N) electrochemical workstation.

### **DFT Calculation Methods**

Theoretical investigations were carried out using the CASTEP package which is based on density functional theory (DFT). The computational method employed the generalized gradient approximation (GGA) with the Perdew–Burke–Ernzerhof parameterization (PBE) for the exchange-correlation function. The kinetic cut-off energy for the plane-wave basis was set to 430 eV, which is used to describe valence electrons in system. The Brillouin-zone integration was sampled with the k-point at 0.05 Å<sup>-1</sup> separations in the reciprocal space. Typically, the band structures and density of states of NiS<sub>2</sub>, NiSe<sub>2</sub>, NiSSe, NiS<sub>1.5</sub>Se<sub>0.5</sub>, and NiS<sub>1.25</sub>Se<sub>0.75</sub> were modeled by the pristine crystal cells.

### **Supporting Information**

Supporting Information is available from the Wiley Online Library or from the author.

### **Acknowledgements**

This work was financially supported by the National Natural Science Foundation of China (Grant Nos. 11974074 and 11804048), the Science and Technology Commission of Shanghai Municipality (18ZR1402000), the Fundamental Research Funds for the Central Universities (2232021D-28), the Program Innovative Research Team in University (IRT\_16R13), and the International Joint Laboratory for Advanced fiber and Low-dimension Materials (18520750400).

### **Conflict of Interest**

The authors declare no conflict of interest.

Received: ((will be filled in by the editorial staff))

Revised: ((will be filled in by the editorial staff))

Published online: ((will be filled in by the editorial staff))

**References**

- [1] Y. Shan, Y. Li, H. Pang, *Adv. Funct. Mater.* **2020**, *30*, 2001298.
- [2] X. Yang, A. L. Rogach, *Adv. Energy Mater.* **2020**, *10*, 2000288.
- [3] J. Ding, W. Hu, E. Paek, D. Mitlin, *Chem. Rev.* **2018**, *118*, 6457.
- [4] H. W. Wang, H. Yi, C. R. Zhu, X. F. Wang, H. J. Fan, *Nano Energy* **2015**, *13*, 658.
- [5] W. H. Li, Z. Z. Yang, M. S. Li, Y. Jiang, X. Wei, X. W. Zhong, L. Gu, Y. Yu, *Nano Lett.* **2016**, *16*, 1546.
- [6] S. S. Yao, J. Cui, J. Q. Huang, J. Huang, W. G. Chong, L. Qin, Y. W. Mai, J. K. Kim, *Adv. Energy Mater.* **2017**, *8*, 1702267.
- [7] Y. Zhang, Q. Su, W. Xu, G. Cao, Y. Wang, A. Pan, S. Liang, *Adv. Sci.* **2019**, *6*, 1900162.
- [8] H. C. Yuan, F. X. Ma, X. B. Wei, J. L. Lan, Y. Liu, Y. H. Yu, X. P. Yang, H. S. Park, *Adv. Energy Mater.* **2020**, *10*, 2001418.
- [9] S. Liu, J. Feng, X. Bian, J. Liu, H. Xu, *Energy Environ. Sci.* **2016**, *9*, 1229.
- [10] J. Liu, Z. Yang, J. Wang, L. Gu, J. Maier, Y. Yu, *Nano Energy* **2015**, *16*, 389.
- [11] Y. Z. Jiang, M. J. Hu, D. Zhang, T. Z. Yuan, W. P. Sun, B. Xu, M. Yan, *Nano Energy* **2014**, *5*, 60.
- [12] Y. Y. Chen, X. D. Hu, B. Evanko, X. H. Sun, X. Li, T. Y. Hou, S. Cai, C. M. Zheng, W. B. Hu, G. D. Stucky, *Nano Energy* **2018**, *46*, 117.
- [13] Z. M. Man, P. Li, D. Zhou, Y. Z. Wang, X. H. Liang, R. Zang, P. X. Li, Y. Q. Zuo, Y. M. Lam, G. X. Wang, *Nano Lett.* **2020**, *20*, 3769.
- [14] Z. Hu, Z. Zhu, F. Cheng, K. Zhang, J. Wang, C. Chen, J. Chen, *Energy Environ. Sci.* **2015**, *8*, 1309.
- [15] S. C. Chen, Z. X. Kang, X. Hu, X. D. Zhang, H. Wang, J. F. Xie, X. S. Zheng, W. S. Yan, B. Pan, Y. Xie, *Adv. Mater.* **2017**, *29*, 1701687.
- [16] C. Wang, T. Y. Wang, J. J. Liu, Y. Zhou, D. W. Yu, J. C. Kuei, F. Han, Q. Li, J. T. Chen, Y. H. Huang, *Energy Environ. Sci.* **2018**, *11*, 2467.
- [17] S. M. Zhou, X. Miao, X. Zhao, C. Ma, Y. Qiu, Z. Hu, J. Zhao, L. Shi, J. Zeng, *Nat. Commun.* **2016**, *7*, 11510.
- [18] S. C. Liang, S. Zhang, Z. Liu, J. Feng, Z. M. Jiang, M. J. Shi, L. Chen, T. Wei, Z. J. Fan, *Adv. Energy Mater.* **2021**, *11*, 2002600.

- [19] C. T. Zhao, C. Yu, M. D. Zhang, Q. Sun, S. F. Li, M. N. Banis, X. T. Han, Q. Dong, J. Yang, G. Wang, X. L. Sun, J. S. Qiu, *Nano Energy* **2017**, *41*, 66.
- [20] J. B. Li, J. L. Li, D. Yan, S. J. Hou, X. T. Xu, T. Lu, Y. F. Yao, W. J. Mai, L. K. Pan, *J. Mater. Chem. A* **2018**, *6*, 6595.
- [21] S. P. Zhang, G. Wang, B. B. Wang, J. M. Wang, J. T. Bai, H. Wang, *Adv. Funct. Mater.* **2020**, *30*, 2001592.
- [22] G. G. Zhao, Y. Zhang, L. Yang, Y. L. Jiang, Y. Zhang, W. W. Hong, Y. Tian, H. B. Zhao, J. G. Hu, L. Zhou, H. S. Hou, X. B. Ji, L. Q. Mai, *Adv. Funct. Mater.* **2018**, *28*, 1803690.
- [23] M. Hu, Z. Ju, Z. Bai, K. Yu, Z. Fang, R. Lv, G. Yu, *Small Methods* **2019**, *4*, 1900673.
- [24] T. S. Wang, P. Hu, C. J. Zhang, H. P. Du, Z. H. Zhang, X. G. Wang, S. G. Chen, J. W. Xiong, G. L. Cui, *ACS Appl. Mater. Interfaces* **2016**, *8*, 7811.
- [25] X. Li, Y. Chen, J. Zou, X. Zeng, L. Zhou, H. Huang, *J. Power Sources* **2016**, *331*, 360.
- [26] H. Fan, H. Yu, X. Wu, Y. Zhang, Z. Luo, H. Wang, Y. Guo, S. Madhavi, Q. Yan, *ACS Appl. Mater. Interfaces* **2016**, *8*, 25261.
- [27] Y. Wang, X. P. Li, M. M. Zhang, Y. G. Zhou, D. W. Rao, C. Zhong, J. F. Zhang, X. P. Han, W. B. Hu, Y. C. Zhang, K. Zaghbi, Y. S. Wang, Y. D. Deng, *Adv. Mater.* **2020**, *32*, 2000231.
- [28] T. S. Wang, D. Legut, Y. C. Fan, J. Qin, X. F. Li, Q. F. Zhang, *Nano Lett.* **2020**, *20*, 8, 6199.
- [29] C. Marini, A. Perucchi, D. Chermisi, P. Dore, M. Valentini, D. Topwal, D. D. Sarma, S. Lupi, P. Postorino, *Phys. Rev. B* **2011**, *84*, 235134.
- [30] B. Yu, X. Q. Wang, F. Qi, B. J. Zheng, J. R. He, J. Lin, W. L. Zhang, Y. R. Li, Y. F. Chen, *ACS Appl. Mater. Interfaces* **2017**, *9*, 7154.
- [31] L. L. Zhai, C. H. Mak, J. S. Qian, S. H. Lin, S. P. Lau, *Electrochim. Acta* **2019**, *305*, 37.
- [32] K. Wang, C. J. Zhou, D. Xia, Z. Q. Shi, C. He, H. Y. Xia, G. W. Liu, G. J. Qiao, *Nano Energy* **2015**, *18*, 1.
- [33] H. J. Meng, W. J. Zhang, Z. Z. Ma, F. Zhang, B. Tang, J. P. Li, X. G. Wang, *ACS Appl. Mater. Interfaces* **2018**, *10*, 2430.
- [34] P. Ge, H. S. Hou, S. J. Li, L. Yang, X. B. Ji, *Adv. Funct. Mater.* **2018**, *28*, 1801765.
- [35] J. P. Sun, X. T. Hu, Z. D. Huang, T. X. Huang, X. K. Wang, H. L. Guo, F. N. Dai, D. F. Sun, *Nano Res.* **2020**, *13*, 2056.
- [36] Q. D. Li, L. Li, P. J. Wu, N. Xu, L. Wang, M. Li, A. Dai, K. Amine, L. Q. Mai, J. Lu, *Adv. Energy Mater.* **2019**, *9*, 1901153.

- [37] S. T. Liu, D. Li, G. J. Zhang, D. D. Sun, J. S. Zhou, H. H. Song, *ACS Appl. Mater. Interfaces* **2018**, *10*, 34193.
- [38] C. Z. Zhang, D. H. Wei, F. Wang, G. H. Zhang, J. F. Duan, F. Han, H. G. Duan, J. S. Liu, *J. Energy Chem.* **2021**, *53*, 24.
- [39] F. Wang, F. Han, Y. L. He, J. Zhang, H. Wu, J. Tao, C. Z. Zhang, F. Q. Zhang, J. S. Liu, *Adv. Funct. Mater.* **2020**, *31*, 2007266.
- [40] C. Z. Zhang, F. Wang, F. Han, H. Wu, F. W. Zhang, G. H. Zhang, J. S. Liu, *Adv. Mater. Interfaces* **2020**, *7*, 2000486.
- [41] P. Ge, S. J. Li, L. Q. Xu, K. Y. Zou, X. Gao, X. Y. Cao, G. Q. Zou, H. S. Hou, X. B. Ji, *Adv. Energy Mater.* **2018**, *9*, 1803035.
- [42] B. H. Hou, Y. Y. Wang, D. S. Liu, Z. Y. Gu, X. Feng, H. S. Fan, T. F. Zhang, C. L. Lu, X. L. Wu, *Adv. Funct. Mater.* **2018**, *28*, 1805444.
- [43] J. B. Li, J. L. Li, D. Yan, S. J. Hou, X. T. Xu, T. Lu, Y. F. Yao, W. J. Mai, L. K. Pan, *J. Mater. Chem. A* **2018**, *6*, 6595.
- [44] T. Brezesinski, J. Wang, S. H. Tolbert, B. Dunn, *Nat. Mater.* **2010**, *9*, 146.
- [45] D. L. Chao, C. R. Zhu, P. H. Yang, X. Xia, J. Liu, J. Wang, X. Fan, S. V. Savilov, J. Y. Lin, H. Fan, Z. X. Shen, *Nat. Commun.* **2016**, *7*, 12122.
- [46] K. Tang, X. Q. Yu, J. P. Sun, H. Li, X. J. Huang, *Electrochim. Acta* **2011**, *56*, 4869.